

Divergence of the normalized wall shear stress as an effective computational template of low-density lipoprotein polarization at the arterial blood-vessel wall interface

*Original*

Divergence of the normalized wall shear stress as an effective computational template of low-density lipoprotein polarization at the arterial blood-vessel wall interface / Mazzi, Valentina; De Nisco, Giuseppe; Calo, Karol; Chiastra, Claudio; Daemen, Joost; Steinman, David A; Wentzel, Jolanda J; Morbiducci, Umberto; Gallo, Diego. - In: COMPUTER METHODS AND PROGRAMS IN BIOMEDICINE. - ISSN 0169-2607. - 226:(2022), p. 107174. [10.1016/j.cmpb.2022.107174]

*Availability:*

This version is available at: 11583/2972986 since: 2022-11-11T14:45:27Z

*Publisher:*

ELSEVIER IRELAND LTD

*Published*

DOI:10.1016/j.cmpb.2022.107174

*Terms of use:*

This article is made available under terms and conditions as specified in the corresponding bibliographic description in the repository

*Publisher copyright*

(Article begins on next page)

# **Divergence of the normalized wall shear stress as an effective computational template of low-density lipoprotein polarization at the arterial blood-vessel wall interface**

Valentina Mazzi<sup>1</sup>, Giuseppe De Nisco<sup>1</sup>, Karol Calò<sup>1</sup>, Claudio Chiastra<sup>1</sup>, Daemen Joost<sup>2</sup>,  
David A. Steiman<sup>3</sup>, Jolanda J. Wentzel<sup>2</sup>, Umberto Morbiducci<sup>1</sup>, Diego Gallo<sup>1†</sup>

<sup>1</sup> *PoliTo<sup>BIO</sup>Med Lab, Department of Mechanical and Aerospace Engineering, Politecnico di Torino, Turin, Italy*

<sup>2</sup> *Department of Cardiology, Biomedical Engineering, Erasmus MC, 3000 CA Rotterdam, The Netherlands*

<sup>3</sup> *Biomedical Simulation Lab, Department of Mechanical and Industrial Engineering, University of Toronto, Toronto, Ontario, Canada*

**†Address for correspondence:**

Diego Gallo, PhD

PoliTo<sup>BIO</sup>Med Lab, Department of Mechanical and Aerospace Engineering

Corso Duca degli Abruzzi, 24 – 10129 Turin, Italy

Tel: +39 011 090 6574

Fax: +39 011 090 6999

Email: [diego.gallo@polito.it](mailto:diego.gallo@polito.it)

**Number of words:** 3978

**Number of figures/tables:** 10

## Abstract

**Background and Objective:** Near-wall transport of low-density lipoprotein (LDL) in arteries plays a relevant role in the initiation of atherosclerosis. Although it can be modelled *in silico* by coupling the Navier–Stokes equations with the 3D advection-diffusion (AD) equation, the associated computational cost is high. As wall shear stress (WSS) represents a first-order approximation of the near-wall velocity in arteries, we aimed at identifying computationally convenient WSS-based quantities to infer LDL near-wall transport based on the underlying near-wall hemodynamics in five models of three human arterial districts (aorta, carotid bifurcations, coronary arteries). The simulated LDL transport and its WSS-based surrogates were qualitatively compared with *in vivo* longitudinal measurements of wall thickness growth on the coronary artery models.

**Methods:** Numerical simulations of blood flow coupled with AD equations for LDL transport and blood-wall transfer were performed. The co-localization of the simulated LDL concentration polarization patterns with luminal surface areas characterized by low cycle-average WSS, near-wall flow stagnation and WSS attracting patterns was quantitatively assessed by the similarity index (SI). In detail, the latter two represent features of the WSS topological skeleton, obtained respectively through the Lagrangian tracking of surface-born particles, and the Eulerian analysis of the divergence of the normalized cycle-average WSS vector field.

**Results:** Convergence of the solution of the AD problem required the simulation of 3 (coronary artery) to 10 (aorta) additional cardiac cycles with respect to the Navier-Stokes problem. Co-localization results underlined that WSS topological skeleton features indicating near-wall flow stagnation and WSS attracting patterns identified LDL concentration polarization profiles more effectively than low WSS, as indicated by higher SI values (SI range: 0.17-0.50 for low WSS; 0.24-0.57 for WSS topological skeleton features). Moreover, the correspondence between the simulated

LDL uptake and WSS-based quantities profiles with the *in vivo* measured wall thickness growth in coronary arteries appears promising.

**Conclusions:** The recently introduced Eulerian approach for identifying WSS attracting patterns from the divergence of normalized WSS provides a computationally affordable template of the LDL polarization at the arterial blood-wall interface without simulating the AD problem. It thus candidates as an effective biomechanical tool for elucidating the mechanistic link among LDL transfer at the arterial blood-wall interface, WSS and atherogenesis.

**Keywords:** Topological skeleton; atherosclerosis; computational fluid dynamics; advection-diffusion; near-wall transport.

## 1. Introduction

It is well established that the altered equilibrium of the transport of biochemicals at the arterial blood-vessel wall interface plays a major role in vascular disease [1–3]. In particular, elevated blood levels of Low-Density Lipoproteins (LDL) increase the risk of atherosclerotic lesions development [4] by LDL penetrating in the subendothelial layer of the arterial wall in regions of endothelial dysfunction, enhancing oxidative stress, inflammation and ultimately the formation of atherosclerotic lesions [5,6].

Transport and blood-vessel wall transfer of biochemicals in patient-specific arteries can be investigated *in silico* by coupling cardiovascular imaging with the numerical solution of the Navier–Stokes (NS) and advection-diffusion (AD) equations [7–11]. The simulation of mass transport in arterial flows is challenged by the fact that (i) such a phenomenon is typically characterized by high Péclet and Schmidt numbers, indicating the predominance of advective vs. diffusive transport, and (ii) most of the relevant biological processes occur in the near-wall region [7], where thin fluid diffusive boundary layers are typically formed [12]. Numerically, this implies that highly resolved computational grids are necessary to properly simulate the transport of biochemicals at the blood-vessel wall interface. The consequent high computational cost [12,13] has hampered the study of biotransport in large populations of patient-specific cardiovascular models, and ultimately the unambiguous interpretation of the flow-related mechanisms regulating blood-vessel wall mass transfer in relation to arterial wall disease. Despite these limitations, a large body of numerical studies supports the existence of a link between near-wall hemodynamics and transport of biochemicals in arteries, highlighting e.g. a correspondence between areas at the luminal surface where LDL concentration polarization occurs and disturbed wall shear stress (WSS) profiles [7,14–20]. Such correspondence is tightly coupled to two mechanisms. First, an altered WSS profile can locally affect the permeability of the endothelium, thus facilitating the transport of biochemicals

into the subendothelial layer [7]. Second, disturbed WSS profiles are typically associated with near-wall flow disturbances such as flow separation and recirculation, which in turn cause an elevated thickness of the diffusive boundary layer at the underlying blood-wall interface.

Recent research has suggested that the computationally burdensome full 3D continuum problem of transport can be reduced to a surface problem by reasonably identifying specific WSS features as surrogate biomechanical markers of LDL concentration polarization [8,20,21]. More in detail, specific quantities based on WSS might provide affordable and computationally-convenient templates of the LDL concentration polarization profiles at the arterial luminal surface without explicitly solving the AD problem. The identification of these WSS-based quantities, informed by fluid mechanics theory, opens to the possibility to further elucidate the associations between LDL transfer at the blood-wall interface, WSS and atherogenesis by addressing some of the impracticalities of analyzing arterial transport phenomena in large datasets of realistic computational hemodynamic models. In this direction, the arterial WSS topological skeleton received considerable interest due to the related interpretation of WSS as a first-order approximation of near-wall velocity [19,21–23], and has been recently proposed as a template for near-wall transport of biochemicals [19,21,24].

The present study aims to use a fast and computationally convenient methodology to prove that WSS topological skeleton is an affordable and quantitative template of LDL distribution at the interface between blood and arterial wall, without resorting to explicitly solving the 3D AD problem. To do that, five personalized computational models of three human vascular districts (aorta, carotid bifurcation, coronary arteries) were considered [25–27]. Computational fluid dynamics (CFD) simulations were performed to solve the NS equations, coupled with AD equations simulating LDL transport and blood-vessel wall transfer. Using the simulated data as reference, the capability in localizing regions of high LDL concentration polarization at the vessel wall of Lagrangian-based

[19,21] and Eulerian-based [22,23] features of the WSS topological skeleton, and of conventional WSS magnitude as well, was tested. The performance of the WSS-based quantities as templates of LDL distribution at the blood-vessel wall interface was analysed in terms of computational costs vs. accuracy. Finally, the soundness of the simulated LDL blood-wall transfer process was assessed by comparison with *in vivo* longitudinal wall thickness (WT) growth data available for the two human coronary artery models.

## 2. Materials and Methods

A schematic diagram of the research methodology adopted in this study is provided in Figure 1 and detailed below.

### 2.1. *Subjects of the study, medical imaging and geometry reconstruction*

The anatomy data of ostensibly healthy human vascular regions (one thoracic aorta, two carotid bifurcations and two coronary arteries) were acquired to build personalized arterial models, as reported in previous studies [25–27]. In detail, the 3D geometry of a ostensibly healthy thoracic aorta (subject S1; Figure 1) was reconstructed from 4D flow MRI acquisitions, as extensively described elsewhere [27–29]. The 3D geometries of the two carotid bifurcations (subjects S2 and S3; Figure 1) were reconstructed from contrast enhanced magnetic resonance angiography (CE-MRA) [25,30]. One right (RCA) and one left anterior descending (LAD) coronary artery (subjects S4 and S5, respectively; Figure 1) were imaged by computed coronary tomography angiography (CCTA) and intravascular ultrasound (IVUS) and the 3D geometries were reconstructed as detailed in previous studies [26,31,44]. The imaging techniques used for the geometry reconstruction of each case are summarized in Table 1. Institutional review board approval was obtained, and all subjects provided informed consent.

### 2.2. *Computational hemodynamics*

Blood flow and LDL transport was simulated by assuming blood as an incompressible Newtonian fluid (density equal to  $1060 \text{ kg m}^{-3}$ ; dynamic viscosity equal to  $3.5 \times 10^{-3} \text{ Pa s}$ ). The 3D unsteady NS equations governing fluid motion in the form:

$$\begin{cases} \nabla \cdot \mathbf{u} = 0 \\ \partial_t \mathbf{u} + (\mathbf{u} \cdot \nabla) \mathbf{u} = -\frac{\nabla p}{\rho} + \nabla \cdot [\nu(\nabla \mathbf{u} + \nabla \mathbf{u}^T)], \end{cases} \quad (1)$$

where  $\mathbf{u}$  is the velocity,  $p$  is the pressure,  $\rho$  is the density and  $\nu$  is the kinematics viscosity, were numerically solved in their discretized form by adopting the finite volume method. To do this, the



CFD code Fluent (ANSYS Inc., USA) was applied to computational grids consisting of tetrahedral elements in the lumen region and 30 layers of high-quality prismatic cells in the near-wall region. The dimensions of the boundary layers was set according to previous studies [9,32]. Conditions at boundaries were prescribed according to the availability of vessel-specific measured data, as summarized in Table 1 and as previously detailed [25–27,31–33]. To ensure a periodic solution without effects linked to initial conditions or transient effects, cardiac cycles were first simulated and discarded until the maximum local percentage difference in WSS between one simulated cardiac cycle and the previous one was lower than 1%.

### 2.3. *Advection-diffusion transport*

To model LDL transport, the NS equations (Eq. 1) were coupled with the AD equation, assuming LDL to be present in dissolved form in blood and modelling it as a passive non-reacting scalar:

$$\frac{dC}{dt} + \mathbf{u} \cdot \nabla C - D_{LDL} \nabla^2 C = 0, \quad (2)$$

where  $C$  is the LDL concentration,  $\mathbf{u}$  is the velocity vector obtained from the solution of Eq. (1), and  $D_{LDL}$  is the diffusivity of LDL in flowing blood, set to a constant value of  $5.983 \cdot 10^{-12} \text{ m}^2 \text{ s}^{-1}$  [15]. To numerically solve LDL transport, the approach proposed by [32] was adopted prescribing a constant LDL concentration at the inlet section ( $C_0 = 2.86 \cdot 10^{-9} \text{ mol m}^{-3}$ ), corresponding to the physiological LDL concentration in whole blood [34]. At each outflow section of the fluid domain, the stress-free condition was applied for LDL. The LDL transfer at the blood-wall interface was modelled by prescribing the following condition at the luminal surface:

$$C_W v_W - D_{LDL} \left. \frac{\partial C}{\partial n} \right|_W = 0, \quad (3)$$

where  $C_W$  is the LDL concentration at the vessel wall,  $v_W$  the filtration velocity through the wall,  $\frac{\partial C}{\partial n}$  is the concentration gradient normal to the vessel wall [15,32]. A uniform LDL concentration equal to  $C_0$  was applied as initial condition to both the fluid domain and the wall [32]. Details on the

meshing strategy, applied numerical schemes and convergence criteria have been provided in previous studies [32]. Simulations of the AD problem were carried out until the maximum local percentage difference in LDL concentration between one simulated cardiac cycle and the previous one was lower than 1%.

#### 2.4. *Templates of LDL concentration polarization and related theoretical framework*

We investigate here whether near-wall transport of LDL can be inferred relying on WSS-based quantities [18,19,21,24] as an alternative to the use of Eqs. (2) and (3). According to the current view, low WSS magnitude (i) directly influences endothelial permeability, thus facilitating the transport of LDL into the subendothelial layer [35], (ii) determines the biochemical flux at the vessel wall [36] and (iii) reflects a thickened diffusive boundary layer for blood-wall mass transfer [1]. Thus, Time-Averaged Wall Shear Stress (TAWSS), defined as:

$$\text{TAWSS} = \frac{1}{T} \int_0^T |\boldsymbol{\tau}| dt, \quad (4)$$

where  $\boldsymbol{\tau} \in \mathbb{R}^3$  is the WSS vector and  $T$  is the cardiac cycle duration, can be adopted as an indicator of luminal surface areas prone to LDL polarization.

More recent research has demonstrated [37] that the WSS can be scaled to provide a first-order approximation for the near-wall blood flow velocity, which governs mass transfer problems, as follows:

$$\mathbf{u}_\pi = \frac{\boldsymbol{\tau} \delta n}{\mu} + O(\delta n^2), \quad (5)$$

where  $\mathbf{u}_\pi \in \mathbb{R}^3$  is the near-wall velocity, and  $\delta n$  is the distance from the wall where  $\mathbf{u}_\pi$  is evaluated. This conceptualized the link between intravascular fluid structures regulating the near-wall biotransport processes like flow separation, stasis or recirculation [23,24], and the contraction (attracting) regions of the WSS topological skeleton, which attract biochemicals in their vicinity leading to locally elevated near-wall concentrations [23,38]. These attracting WSS regions can be

obtained by extending the calculation of Coherent Structures (CS), typically computed from the velocity vector field to highlight complex flow features, to WSS (referred to in the following as WSS CS) to provide a template of near-wall transport of biochemicals, as previously proposed [8,19,21,24]. In this regard, a sketch linking WSS field in a contraction configuration, near-wall velocity streamlines and diffusive boundary layer where flow separation (leading to recirculating flow) occurs, is depicted in Figure 2A. Near-wall trajectories of biochemicals tend to be attracted and accumulate where WSS is characterized by an attracting pattern, leading to elevated local near-wall concentration of biochemicals (Figure 2B). To better clarify the physics of the phenomenon, we remind here that in correspondence of a WSS contraction region a component of the near-wall velocity directed normal to the wall is indeed present (Figure 2A), but such component is second order in  $\delta n$ , as can be argued from Eq. (5) [37]. Thus, the contribution of near-wall tangential velocity is dominant (first order in  $\delta n$ ) and the thick diffusive boundary layer in WSS contraction regions hinders near-wall trajectories to escape the boundary layer.

Computationally, attracting WSS CS can be identified by Lagrangian particle tracking, i.e. integrating surface tracers based on the near-wall blood flow velocity (Eq. 5) and identifying the formed material lines, as proposed and extensively described elsewhere [19,21]. The tracked Lagrangian trajectories of the surface-born tracers can be used to evaluate the WSS exposure time ( $WSS_{EX}$ ), a descriptor accounting for near-wall biochemicals stagnation/redistribution [19,21]:

$$WSS_{EX}(e) = \frac{1}{\theta} \sqrt{\frac{\bar{A}}{A_e}} \sum_{p=1}^{N_t} \int_0^{\theta} \mathbb{I}_e(\mathbf{x}_p, t) dt, \quad (6)$$

where  $e$  is the generic triangular element of the mesh of area  $A_e$ ,  $\bar{A}$  is the average surface area of all surface triangles of the mesh,  $\mathbf{x}_p(t)$  is the position of the WSS trajectory,  $\mathbb{I}_e$  is the indicator function for element  $e$ ,  $N_t$  is the total number of trajectories released, and  $\theta$  is the integration time.

Equation (6) quantifies the accumulated amount of time that near-wall biochemicals spend in that region [19], thus characterizing near-wall transport.

Exploiting the quasi-steady nature of near-wall transport in cardiovascular flows, recent studies [19,21] have demonstrated that attracting Lagrangian WSS CS match the unstable critical lines (manifolds) of the WSS field, suggesting that unstable critical lines of the cycle-average WSS field can mark where LDL concentration polarization preferentially occurs at the luminal surface. This approach significantly reduces the computational effort, as the WSS topological skeleton unstable critical lines can be identified directly from the cycle-average WSS field via direct numerical integration, without having to solve the Lagrangian surface transport [19,21]. However, unstable critical lines per se [19,21,23] do not allow a fully quantitative analysis of the extension of regions where local LDL concentration polarization may occur. An example of an unstable critical line and its correspondence with the attracting WSS CS is shown in Fig. 2B.

To overcome these limitations, attracting WSS CS and unstable WSS manifolds can be obtained by applying a Eulerian-based approach, recently proposed for the characterization of the WSS topological skeleton [22,23]. In detail, based on the volume contraction theory, highly negative values of the divergence of the normalized cycle-average WSS vector field defined as:

$$\text{DIV}_{\text{WSS}} = \nabla \cdot \left( \frac{\bar{\boldsymbol{\tau}}}{\|\bar{\boldsymbol{\tau}}\|_2} \right), \quad (7)$$

can be used as a robust approximation of attracting WSS CS and unstable cycle-average WSS critical lines [22,23,39–43].

## 2.5. Performance evaluation of WSS-based quantities as templates of LDL concentration

The quantitative analysis of the co-localization between low WSS regions, near-wall stagnation (as indicated by  $\text{WSS}_{\text{EX}}$ ), WSS contraction regions (as indicated by  $\text{DIV}_{\text{WSS}}$ ) and local LDL concentration polarization was carried out by the following scheme. First, surface areas (SAs) exposed to low WSS, near-wall stagnation, WSS contraction regions and high local LDL uptake were identified by

computing objective thresholds corresponding to the subject-specific 10<sup>th</sup> percentiles of the distribution of TAWSS and of the signed quantity  $DIV_{WSS}$  (whose 10<sup>th</sup> percentile includes only negative  $DIV_{WSS}$  values), and 90<sup>th</sup> percentiles for  $WSS_{EX}$  and LDL concentration. Luminal SAs below ( $TAWSS$ ,  $DIV_{WSS}$ ) or above ( $WSS_{EX}$ , LDL concentration) these thresholds were named as TAWSS10, DIV10, WSSEX90, and LDL90, respectively. The quantities considered in this study and their link with near-wall transport of biochemicals and biologically relevant events are summarized in Table 2. The ability of the hemodynamic quantities to identify local LDL uptake was then assessed by the Similarity Index (SI) [33]:

$$SI = \frac{2(SA_{LDL90} \cap SA_j)}{SA_{LDL90} \cup SA_j} \quad (8)$$

with  $j = TAWSS10, DIV10, WSSEX90$ . SI ranges from 0 (the SAs given by the two quantities have no spatial overlap) to 1 (the SAs are equivalent and perfectly spatially overlapped).

## 2.6. Wall Thickness Measurements

Longitudinal *in vivo* coronary artery WT growth measurements, a hallmark of atherosclerosis development, were available for subjects S4 and S5 [44] and used to check the capability of the here considered WSS-based quantities and LDL concentration to identify locations of possible lesion growth. In detail, the maps of local WT on the two coronary arteries were obtained from IVUS images acquired at baseline ( $T_1$ ) and repeated at 12 months follow-up ( $T_2$ ) by using a semi-automatic method for lumen and vessel wall contour detection [39,44]. Technically, WT was locally measured by subtracting the local lumen radius to the local outer wall radius, as schematized in Figure 1 [44]. From WT data at  $T_1$  and  $T_2$  ( $WT_1$  and  $WT_2$ , respectively), the WT growth normalized for the baseline WT was defined as  $\Delta WT / WT_1 = (WT_2 - WT_1) / WT_1$ .

### 3. Results

In Figure 3 luminal LDL concentration profiles are compared with the distribution of WSS-based quantities (TAWSS,  $DIV_{WSS}$ , and  $WSS_{EX}$ ). It can be observed by visual inspection that in general LDL luminal concentration polarization patterns (high  $C_W/C_0$  values) co-localize differently with patterns of WSS-based quantities. The co-localization is particularly evident at: (i) the origin of the brachiocephalic artery, the inner curve of the aortic arch and along the descending aorta for the aortic model (S1, Figure 3); (ii) the carotid bulb and the outer wall of the external carotid artery for carotid bifurcations (S2, S3; Figure 3); (iii) the inner curvature of coronary arteries (S4, S5; Figure 3). For each investigated artery, LDL concentration polarization profiles and WSS-based quantities distribution along the two luminal cross-sections characterized by the highest values of  $C_W/C_0$  are presented in Figure 4 as explanatory cases to emphasize the capability of TAWSS,  $DIV_{WSS}$  and  $WSS_{EX}$  of identifying regions of high  $C_W/C_0$  at the luminal surface.

To better appreciate the capability of the WSS-based quantities to identify regions of elevated local LDL uptake, luminal SAs exposed to TAWSS10,  $DIV_{10}$  and  $WSSEX_{90}$  are visualized together with LDL90 SAs (Figure 5). In general, the analysis highlights a remarkable spatial overlap of LDL90 SAs with  $DIV_{10}$  and  $WSSEX_{90}$  SAs in all the cases under study, and a good overlap of LDL90 SAs with TAWSS10 SAs.

These qualitative observations are confirmed by the quantitative analysis based on the calculation of the SI (Table 3), highlighting a remarkable co-localization between  $DIV_{10}$  or  $WSSEX_{90}$  SAs and LDL90 SAs in all the vessels under investigation, going from a minimum of  $SI=0.24$  (subject S5) to a maximum of  $SI=0.53$  and  $SI=0.57$  for  $DIV_{10}$  and  $WSSEX_{90}$ , respectively (subject S3). However, TAWSS10 SAs exhibits weaker co-localization with LDL90 SAs, with SI values ranging from 0.17 (subject S5) to 0.50 (subject S3). The results summarized in Table 3 suggest that: (i) LDL arterial luminal concentration polarization patterns appear to be associated more strongly to WSS

topological features than WSS magnitude; (ii) profiles of these WSS topological features (from both Lagrangian-based and Eulerian-based analysis) candidates as effective quantitative templates of LDL uptake on the arterial wall.

To obtain a quantitative indication of the computational cost, the number of cardiac cycles required to ensure convergence of the NS and AD solutions is reported in Table 4. Once convergence of the NS solution is reached, the number of additional cardiac cycles to ensure convergence of the AD solution ranges from 3 (right coronary artery, S4) to 10 (thoracic aorta S1, Table 4). Since  $WSS_{EX}$  and  $DIV_{WSS}$  can be obtained from the solution of the NS equations, their use as templates of LDL transfer is markedly computationally less expensive than explicitly solving the full transport problem. When comparing  $WSS_{EX}$  and  $DIV_{WSS}$ , the Lagrangian nature of the former [19] leads to increased computational costs when compared to the latter Eulerian quantity [22]. In particular,  $DIV_{WSS}$  can be computed directly from the NS solution with trivial computational effort and thus can be more readily obtained than  $WSS_{EX}$ .

Finally, the simulated distributions of LDL uptake and WSS-based quantities on coronary artery models (subjects S4 and S5) are compared with the *in vivo* measured WT growth in Figure 6. In general, luminal surface areas with LDL concentration polarization, low WSS, WSS contraction regions and high near-wall stagnation co-localize with regions exhibiting the highest WT growth, even if at different levels (Figure 6).

## 4. Discussion

Near-wall transport has a pivotal role in cardiovascular pathophysiology [36], with the mechanisms linking near-wall hemodynamics to LDL uptake being particularly relevant in the context of atherosclerosis [7,8,15,18,19]. Numerical simulations allow to model local hemodynamics and near-wall transport of LDL in realistic, personalized cardiovascular models, improving the understanding of the link between flow disturbances, LDL transport near and at the vessel wall, and atherosclerosis initiation and progression. However, high-fidelity numerical simulations of near-wall transport in arterial flows might be cumbersome, numerically challenging and extremely expensive in terms of computational effort [12]. For this reason, the identification of simple surrogate measures able to infer near-wall transport based on the underlying near-wall hemodynamics is of great importance. Here we tested different strategies to obtain affordable templates of LDL concentration polarization profiles at the luminal surface of arteries that do not require the solution of the 3D AD problem for LDL transport. More in detail, the distribution of WSS magnitude at the luminal surface as well as of features extracted from Lagrangian-based [19] and Eulerian-based [22] analysis of the WSS topological skeleton in five subject-specific computational hemodynamic models of human arteries was compared with simulated LDL uptake data, as obtained from the solution of the 3D coupled NS-AD problem. In addition, for “consistency check” purposes, the simulated LDL concentration polarization and the profiles of the WSS-based quantities were qualitatively compared with WT growth *in vivo* measurements, available from previous follow up studies on the two human coronary artery models [31,44].

The capability of WSS Lagrangian-based quantity  $WSS_{EX}$  as template of LDL concentration polarization profile at the arterial wall was previously reported in terms of correlation with LDL concentration in various arterial domain considering all the data points on the surface [19]. Here, we extended the analysis with quantitative results on the co-localization of their extrema.



Furthermore, the divergence of the normalized WSS field was here tested for the first time as template of LDL concentration polarization profile at the luminal surface, based on its recently demonstrated capability of approximating the manifolds of the WSS topological skeleton [22,23,39]. As a further novel point, the existence of possible links between  $WSS_{EX}$  and  $DIV_{WSS}$  with biological events was checked for the first time considering *in vivo* WT growth data, although qualitatively. The performance of the here-investigated WSS-based quantities in providing affordable templates of the LDL concentration polarization profiles at the arterial luminal surface was evaluated in terms of computational cost and accuracy. The main findings are schematized in Figure 7. The reference target for the LDL concentration polarization profiles is obtained through the numerical solution of the fully 3D NS-AD problem, assumed to model the LDL transport and blood-wall transfer with the highest accuracy. The co-localization of simulated LDL concentration polarization profiles with *in vivo* WT growth in coronary arteries support the biological relevance of this choice. However, the highest accuracy comes at the expense of the computational cost, since additional cardiac cycles have to be simulated (Table 4) in addition to the stringent numerical settings involved in accurately resolving the concentration boundary layer. Interestingly, the number of additional cardiac cycles to ensure convergence of the AD solution appears to increase with the Péclet number, i.e. the predominance of advective vs. diffusive transport, which is higher in the thoracic aorta than in the carotid arteries and in both cases is higher than in the coronary arteries (from 3 additional cycles required by the RCA model to 10 in the case of aorta). This finding could be attributed to the fact that at a higher Péclet number corresponds a thinner concentration boundary layer, requiring a larger number of cardiac cycles to be simulated to meet the convergence criterion. Moreover, in larger arteries the computational costs might be exacerbated by the larger fluid domain to be simulated, as well as by the fact that, e.g., the hemodynamics in the thoracic aorta can be more complex than in the carotid bifurcation, which in turn can be more complex than in coronary

arteries. The WSS topological skeleton features from Lagrangian-based and Eulerian-based analysis exhibited a comparable accuracy in localizing luminal surface areas prone to LDL concentration polarization in terms of SI (going from a minimum of  $SI=0.24$  to a maximum of  $SI=0.53$  for DIV10, and from a minimum of  $SI=0.24$  to a maximum of  $SI=0.57$  for WSSEX90, Table 3 and Figure 5), but with a remarkable reduction in terms of computational cost with respect to the solution of the AD problem, since they are based on the NS solution only (Figure 7). The difference in the computational costs between  $WSS_{EX}$  and  $DIV_{WSS}$  can be explained reminding that  $WSS_{EX}$  is computed from Lagrangian tracking of a large number of particle trajectories, requiring higher-order integration schemes [45,46], while  $DIV_{WSS}$  is computationally less expensive by reason of its Eulerian-based method of analysis. Low WSS magnitude (low TAWSS) underperformed the other WSS-based quantities in localizing LDL concentration polarization on the luminal surface in terms of accuracy (going from a minimum of  $SI=0.17$  to a maximum of  $SI=0.50$ , Table 3 and Figure 5), although its calculation in CFD postprocessing presents the lowest computational cost (Figure 7).

This study faces possible limitations. Here five subject-specific computational models of human arteries were considered to test the technical soundness of the proposed methodology. Larger vessel-specific datasets will be analysed in the future to confirm the reported findings. Regarding the numerical simulations, the modelling assumptions/idealizations (e.g., Newtonian behaviour of blood and vascular rigid walls) might influence local hemodynamics and LDL transport [47,48]. In particular, modelling assumptions related to the rheological behaviour of blood flowing in coronary arteries may impact WSS-based quantities [49] as well as LDL uptake, even if the adoption of Newtonian vs. non-Newtonian constitutive models for blood rheology is still debated [50,51]. Moreover, the prescribed LDL concentration initial conditions could affect the results of LDL transport simulations and, consequently, the relation between WSS features and LDL transfer [32].

Because of these limitations, future studies are warranted to further confirm the robustness of WSS topological skeleton features as templates of near-wall transport of biochemicals in arteries.

Post-Print

## 5. Conclusions

The present study confirms that WSS topological skeleton CS can be used as templates of the LDL transport at the arterial blood-vessel wall interface [19]. The study also suggests that a recently introduced Eulerian approach for identifying WSS topological skeleton features from the WSS divergence [22,23] is effective in providing a representation of the LDL wall uptake with a remarkable reduction in computational costs, not only with respect to classical NS-AD mass transport simulations, but also with respect to WSS CS identification based upon a Lagrangian analysis. The here-proposed approach based on normalized WSS divergence can be easily applied to large-scale datasets of CFD models of arterial flows and used to elucidate the mechanistic link existing among LDL transfer at the blood-vessel wall interface, WSS and atherogenesis.

## Conflict of Interest

The authors state no conflict of interest for the study object of the manuscript. The research was not supported financially by private companies. None of the authors has a financial agreement with peoples or organizations that could inappropriately influence their work.

## Financial support

VM, GDN, KC, CC, UM and DG were supported by the Italian Ministry of Education, University and Research (FISR2019\_03221 , CECOMES). JW was supported by the European Research Council (grant number 310457).

## Acknowledgements

The Authors wish to thank Giovanna Rizzo for the technical support.

## References

- [1] C.G. Caro, J.M. Fitz-Gerald, R.C. Schroter, Atheroma and arterial wall shear. Observation, correlation and proposal of a shear dependent mass transfer mechanism for atherogenesis., *Proc. R. Soc. London. Ser. B, Biol. Sci.* 177 (1971) 109–159. <https://doi.org/10.1098/rspb.1971.0019>.
- [2] G.S. Getz, An overview of atherosclerosis: a look to the future., *Toxicol. Pathol.* 18 (1990) 623–635.
- [3] H.C. Stary, A.B. Chandler, S. Glagov, J.R. Guyton, W.J. Insull, M.E. Rosenfeld, S.A. Schaffer, C.J. Schwartz, W.D. Wagner, R.W. Wissler, A definition of initial, fatty streak, and intermediate lesions of atherosclerosis. A report from the Committee on Vascular Lesions of the Council on Arteriosclerosis, American Heart Association., *Circulation.* 89 (1994) 2462–2478. <https://doi.org/10.1161/01.cir.89.5.2462>.
- [4] L.B. Nielsen, Transfer of low density lipoprotein into the arterial wall and risk of atherosclerosis, *Atherosclerosis.* 123 (1996) 1–15. [https://doi.org/https://doi.org/10.1016/0021-9150\(96\)05802-9](https://doi.org/https://doi.org/10.1016/0021-9150(96)05802-9).
- [5] R. Ross, Rous-Whipple Award Lecture. Atherosclerosis: a defense mechanism gone awry., *Am. J. Pathol.* 143 (1993) 987–1002.
- [6] S. Parthasarathy, D. Steinberg, J.L. Witztum, The role of oxidized low-density lipoproteins in the pathogenesis of atherosclerosis., *Annu. Rev. Med.* 43 (1992) 219–225. <https://doi.org/10.1146/annurev.me.43.020192.001251>.
- [7] C.R. Ethier, Computational modeling of mass transfer and links to atherosclerosis., *Ann. Biomed. Eng.* 30 (2002) 461–471.
- [8] M. Mahmoudi, A. Farghadan, D. McConnell, A.J. Barker, J.J. Wentzel, M.J. Budoff, A. Arzani, The Story of Wall Shear Stress in Coronary Artery Atherosclerosis: Biochemical Transport and Mechanotransduction, *J. Biomech. Eng.* (2020). <https://doi.org/10.1115/1.4049026>.
- [9] X. Li, X. Liu, P. Zhang, C. Feng, A. Sun, H. Kang, X. Deng, Y. Fan, Numerical simulation of haemodynamics and low-density lipoprotein transport in the rabbit aorta and their correlation with atherosclerotic plaque thickness., *J. R. Soc. Interface.* 14 (2017). <https://doi.org/10.1098/rsif.2017.0140>.
- [10] X. Liu, F. Pu, Y. Fan, X. Deng, D. Li, S. Li, A numerical study on the flow of blood and the transport of LDL in the human aorta: the physiological significance of the helical flow in the aortic arch., *Am. J. Physiol. Heart Circ. Physiol.* 297 (2009) H163-70. <https://doi.org/10.1152/ajpheart.00266.2009>.
- [11] X. Liu, Z. Wang, P. Zhao, Z. Fan, A. Sun, F. Zhan, Y. Fan, X. Deng, Nitric oxide transport in normal human thoracic aorta: effects of hemodynamics and nitric oxide scavengers., *PLoS One.* 9 (2014) e112395. <https://doi.org/10.1371/journal.pone.0112395>.
- [12] K.B. Hansen, S.C. Shadden, A reduced-dimensional model for near-wall transport in cardiovascular flows, *Biomech. Model. Mechanobiol.* 15 (2016) 713–722. <https://doi.org/10.1007/s10237-015-0719-4>.
- [13] S. Tada, Numerical study of oxygen transport in a carotid bifurcation., *Phys. Med. Biol.* 55 (2010) 3993–4010. <https://doi.org/10.1088/0031-9155/55/14/004>.
- [14] J. Lantz, M. Karlsson, Large eddy simulation of LDL surface concentration in a subject specific human aorta., *J. Biomech.* 45 (2012) 537–542. <https://doi.org/10.1016/j.jbiomech.2011.11.039>.
- [15] S. Wada, T. Karino, Theoretical prediction of low-density lipoproteins concentration at the luminal surface of an artery with a multiple bend., *Ann. Biomed. Eng.* 30 (2002) 778–791. <https://doi.org/10.1114/1.1495868>.

- [16] N. Sun, N.B. Wood, A.D. Hughes, S.A.M. Thom, X.Y. Xu, Fluid-wall modelling of mass transfer in an axisymmetric stenosis: effects of shear-dependent transport properties., *Ann. Biomed. Eng.* 34 (2006) 1119–1128. <https://doi.org/10.1007/s10439-006-9144-2>.
- [17] H.W. Sill, Y.S. Chang, J.R. Artman, J.A. Frangos, T.M. Hollis, J.M. Tarbell, Shear stress increases hydraulic conductivity of cultured endothelial monolayers., *Am. J. Physiol.* 268 (1995) H535–43. <https://doi.org/10.1152/ajpheart.1995.268.2.H535>.
- [18] U. Olgac, V. Kurtcuoglu, D. Poulikakos, Computational modeling of coupled blood-wall mass transport of LDL: effects of local wall shear stress., *Am. J. Physiol. Heart Circ. Physiol.* 294 (2008) H909–19. <https://doi.org/10.1152/ajpheart.01082.2007>.
- [19] A. Arzani, A.M. Gambaruto, G. Chen, S.C. Shadden, Wall shear stress exposure time: a Lagrangian measure of near-wall stagnation and concentration in cardiovascular flows., *Biomech. Model. Mechanobiol.* 16 (2017) 787–803. <https://doi.org/10.1007/s10237-016-0853-7>.
- [20] U. Olgac, D. Poulikakos, S.C. Saur, H. Alkadhi, V. Kurtcuoglu, Patient-specific three-dimensional simulation of LDL accumulation in a human left coronary artery in its healthy and atherosclerotic states., *Am. J. Physiol. Heart Circ. Physiol.* 296 (2009) H1969–82. <https://doi.org/10.1152/ajpheart.01182.2008>.
- [21] A. Arzani, A.M. Gambaruto, G. Chen, S.C. Shadden, Lagrangian wall shear stress structures and near-wall transport in high-Schmidt-number aneurysmal flows, *J. Fluid Mech.* 790 (2016) 158–172. <https://doi.org/10.1017/jfm.2016.6>.
- [22] V. Mazzi, D. Gallo, K. Calò, M. Najafi, M.O. Khan, G. De Nisco, D.A. Steinman, U. Morbiducci, A Eulerian method to analyze wall shear stress fixed points and manifolds in cardiovascular flows, *Biomech. Model. Mechanobiol.* 19 (2020) 1403–1423. <https://doi.org/10.1007/s10237-019-01278-3>.
- [23] V. Mazzi, U. Morbiducci, K. Calò, G. De Nisco, M. Lodi Rizzini, E. Torta, G.C.A. Caridi, C. Chiastra, D. Gallo, Wall Shear Stress Topological Skeleton Analysis in Cardiovascular Flows: Methods and Applications, *Mathematics*. 9 (2021). <https://doi.org/10.3390/math9070720>.
- [24] A. Farghadan, A. Arzani, The combined effect of wall shear stress topology and magnitude on cardiovascular mass transport, *Int. J. Heat Mass Transf.* 131 (2019) 252–260. <https://doi.org/10.1016/j.ijheatmasstransfer.2018.11.051>.
- [25] D. Gallo, P.B. Bijari, U. Morbiducci, Y. Qiao, Y.J. Xie, M. Etesami, D. Habets, E.G. Lakatta, B.A. Wasserman, D.A. Steinman, Segment-specific associations between local haemodynamic and imaging markers of early atherosclerosis at the carotid artery: an in vivo human study., *J. R. Soc. Interface*. 15 (2018). <https://doi.org/10.1098/rsif.2018.0352>.
- [26] E.M.J. Hartman, G. De Nisco, A.M. Kok, A. Hoogendoorn, A. Coenen, F. Mastik, S.-A. Korteland, K. Nieman, F.J.H. Gijzen, A.F.W. van der Steen, J. Daemen, J.J. Wentzel, Lipid-rich Plaques Detected by Near-infrared Spectroscopy Are More Frequently Exposed to High Shear Stress, *J. Cardiovasc. Transl. Res.* (2020). <https://doi.org/10.1007/s12265-020-10072-x>.
- [27] U. Morbiducci, R. Ponzini, D. Gallo, C. Bignardi, G. Rizzo, Inflow boundary conditions for image-based computational hemodynamics: impact of idealized versus measured velocity profiles in the human aorta., *J. Biomech.* 46 (2013) 102–109. <https://doi.org/10.1016/j.jbiomech.2012.10.012>.
- [28] D. Gallo, G. De Santis, F. Negri, D. Tresoldi, R. Ponzini, D. Massai, M.A. Deriu, P. Segers, B. Verheghe, G. Rizzo, U. Morbiducci, On the use of in vivo measured flow rates as boundary conditions for image-based hemodynamic models of the human aorta: implications for indicators of abnormal flow., *Ann. Biomed. Eng.* 40 (2012) 729–741. <https://doi.org/10.1007/s10439-011-0431-1>.
- [29] P. Volonghi, D. Tresoldi, M. Cadioli, A.M. Uselli, R. Ponzini, U. Morbiducci, A. Esposito, G.

- Rizzo, Automatic extraction of three-dimensional thoracic aorta geometric model from phase contrast MRI for morphometric and hemodynamic characterization., *Magn. Reson. Med.* 75 (2016) 873–882. <https://doi.org/10.1002/mrm.25630>.
- [30] D.A. Steinman, J.B. Thomas, H.M. Ladak, J.S. Milner, B.K. Rutt, J. David Spence, Reconstruction of carotid bifurcation hemodynamics and wall thickness using computational fluid dynamics and MRI, *Magn. Reson. Med.* 47 (2002) 149–159. <https://doi.org/10.1002/mrm.10025>.
- [31] G. De Nisco, C. Chiastra, E.M.J. Hartman, A. Hoogendoorn, J. Daemen, K. Calò, D. Gallo, U. Morbiducci, J.J. Wentzel, Comparison of Swine and Human Computational Hemodynamics Models for the Study of Coronary Atherosclerosis, *Front. Bioeng. Biotechnol.* 9 (2021). <https://doi.org/10.3389/fbioe.2021.731924>.
- [32] G. De Nisco, P. Zhang, K. Calò, X. Liu, R. Ponzini, C. Bignardi, G. Rizzo, X. Deng, D. Gallo, U. Morbiducci, What is needed to make low-density lipoprotein transport in human aorta computational models suitable to explore links to atherosclerosis? Impact of initial and inflow boundary conditions., *J. Biomech.* 68 (2018) 33–42. <https://doi.org/10.1016/j.jbiomech.2017.12.009>.
- [33] D. Gallo, D.A. Steinman, U. Morbiducci, Insights into the co-localization of magnitude-based versus direction-based indicators of disturbed shear at the carotid bifurcation., *J. Biomech.* 49 (2016) 2413–2419. <https://doi.org/10.1016/j.jbiomech.2016.02.010>.
- [34] N. Yang, K. Vafai, Modeling of low-density lipoprotein (LDL) transport in the artery—effects of hypertension, *Int. J. Heat Mass Transf.* 49 (2006) 850–867. <https://doi.org/https://doi.org/10.1016/j.ijheatmasstransfer.2005.09.019>.
- [35] P.D. Weinberg, Haemodynamic Wall Shear Stress, Endothelial Permeability and Atherosclerosis-A Triad of Controversy., *Front. Bioeng. Biotechnol.* 10 (2022) 836680. <https://doi.org/10.3389/fbioe.2022.836680>.
- [36] J.M. Tarbell, Mass transport in arteries and the localization of atherosclerosis., *Annu. Rev. Biomed. Eng.* 5 (2003) 79–118. <https://doi.org/10.1146/annurev.bioeng.5.040202.121529>.
- [37] A.M. Gambaruto, D.J. Doorly, T. Yamaguchi, Wall shear stress and near-wall convective transport: Comparisons with vascular remodelling in a peripheral graft anastomosis, *J. Comput. Phys.* 229 (2010) 5339–5356. <https://doi.org/10.1016/j.jcp.2010.03.029>.
- [38] A. Arzani, S.C. Shadden, Wall shear stress fixed points in cardiovascular fluid mechanics, *J. Biomech.* 73 (2018) 145–152. <https://doi.org/10.1016/j.jbiomech.2018.03.034>.
- [39] V. Mazzi, G. De Nisco, A. Hoogendoorn, K. Calò, C. Chiastra, D. Gallo, D.A. Steinman, J.J. Wentzel, U. Morbiducci, Early Atherosclerotic Changes in Coronary Arteries are Associated with Endothelium Shear Stress Contraction/Expansion Variability, *Ann. Biomed. Eng.* (2021). <https://doi.org/10.1007/s10439-021-02829-5>.
- [40] G. De Nisco, P. Tasso, K. Calò, V. Mazzi, D. Gallo, F. Condemi, S. Farzaneh, S. Avril, U. Morbiducci, Deciphering ascending thoracic aortic aneurysm hemodynamics in relation to biomechanical properties, *Med. Eng. Phys.* 82 (2020) 119–129. <https://doi.org/10.1016/j.medengphy.2020.07.003>.
- [41] U. Morbiducci, V. Mazzi, M. Domanin, G. De Nisco, C. Vergara, D.A. Steinman, D. Gallo, Wall Shear Stress Topological Skeleton Independently Predicts Long-Term Restenosis After Carotid Bifurcation Endarterectomy, *Ann. Biomed. Eng.* 48 (2020) 2936–2949. <https://doi.org/10.1007/s10439-020-02607-9>.
- [42] A. Candreva, M. Pagnoni, M.L. Rizzini, T. Mizukami, E. Gallinoro, V. Mazzi, D. Gallo, D. Meier, T. Shinke, J.-P. Aben, S. Nagumo, J. Sonck, D. Munhoz, S. Fournier, E. Barbato, W. Heggermont, S. Cook, C. Chiastra, U. Morbiducci, B. De Bruyne, O. Muller, C. Collet, Risk of myocardial infarction based on endothelial shear stress analysis using coronary angiography., *Atherosclerosis*. 342 (2022) 28–35. <https://doi.org/10.1016/j.atherosclerosis.2021.11.010>.



- [43] C. Chiastra, V. Mazzi, M. Lodi Rizzini, K. Calò, A. Corti, A. Acquasanta, G. De Nisco, D. Belliggiano, E. Cerrato, D. Gallo, U. Morbiducci, Coronary Artery Stenting Affects Wall Shear Stress Topological Skeleton, *J. Biomech. Eng.* 144 (2022). <https://doi.org/10.1115/1.4053503>.
- [44] E.M.J. Hartman, G. De Nisco, F.J.H. Gijzen, S.-A. Korteland, A.F.W. van der Steen, J. Daemen, J.J. Wentzel, The definition of low wall shear stress and its effect on plaque progression estimation in human coronary arteries, *Sci. Rep.* 11 (2021) 22086. <https://doi.org/10.1038/s41598-021-01232-3>.
- [45] M. Tambasco, D.A. Steinman, On assessing the quality of particle tracking through computational fluid dynamic models., *J. Biomech. Eng.* 124 (2002) 166–175. <https://doi.org/10.1115/1.1449489>.
- [46] P.J. Nolan, M. Serra, S.D. Ross, Finite-time Lyapunov exponents in the instantaneous limit and material transport, *Nonlinear Dyn.* 100 (2020) 3825–3852. <https://doi.org/10.1007/s11071-020-05713-4>.
- [47] X. Liu, Y. Fan, X. Deng, F. Zhan, Effect of non-Newtonian and pulsatile blood flow on mass transport in the human aorta., *J. Biomech.* 44 (2011) 1123–1131. <https://doi.org/10.1016/j.jbiomech.2011.01.024>.
- [48] C.A. Taylor, D.A. Steinman, Image-based modeling of blood flow and vessel wall dynamics: Applications, methods and future directions: Sixth international bio-fluid mechanics symposium and workshop, March 28–30, 2008 Pasadena, California, *Ann. Biomed. Eng.* 38 (2010) 1188–1203. <https://doi.org/10.1007/s10439-010-9901-0>.
- [49] M.C. Fernandes, L.C. Sousa, C.F. de Castro, J.M.L.M. da Palma, C.C. António, S.I.S. Pinto, Implementation and Comparison of Non-Newtonian Viscosity Models in Hemodynamic Simulations of Patient Coronary Arteries, in: I. Giorgio, L. Placidi, E. Barchiesi, B.E. Abali, H. Altenbach (Eds.), *Theor. Anal. Comput. Exp. Multiscale Mater. A Tribut. to Fr. Dell’Isola*, Springer International Publishing, Cham, 2022: pp. 403–428. [https://doi.org/10.1007/978-3-031-04548-6\\_19](https://doi.org/10.1007/978-3-031-04548-6_19).
- [50] M. Iasiello, K. Vafai, A. Andreozzi, N. Bianco, Analysis of non-Newtonian effects on Low-Density Lipoprotein accumulation in an artery., *J. Biomech.* 49 (2016) 1437–1446. <https://doi.org/10.1016/j.jbiomech.2016.03.017>.
- [51] A. Arzani, Accounting for residence-time in blood rheology models: do we really need non-Newtonian blood flow modelling in large arteries?, *J. R. Soc. Interface.* 15 (2018). <https://doi.org/10.1098/rsif.2018.0486>.



**Figure 1. Schematic diagram of the study design.** In vivo imaging is adopted to reconstruct the 3D geometries of the human arteries adopted in this study. In vivo imaging and intravascular measurements are used to set personalized boundary conditions in CFD simulations. After solving the NS equations, (i) the AD problem of the LDL transport is numerically solved, and (ii) the WSS-based quantities are computed by postprocessing the resolved flow field. A descriptive sketch of the approach used to obtain *in vivo* wall thickness measurements from IVUS images is also reported. MRI: magnetic resonance imaging; CCTA: coronary computed tomography angiography; IVUS: intravascular ultrasound; NS: Navier-Stokes; AD: advection-diffusion; LDL: Low-Density Lipoproteins; WSS: wall shear stress.

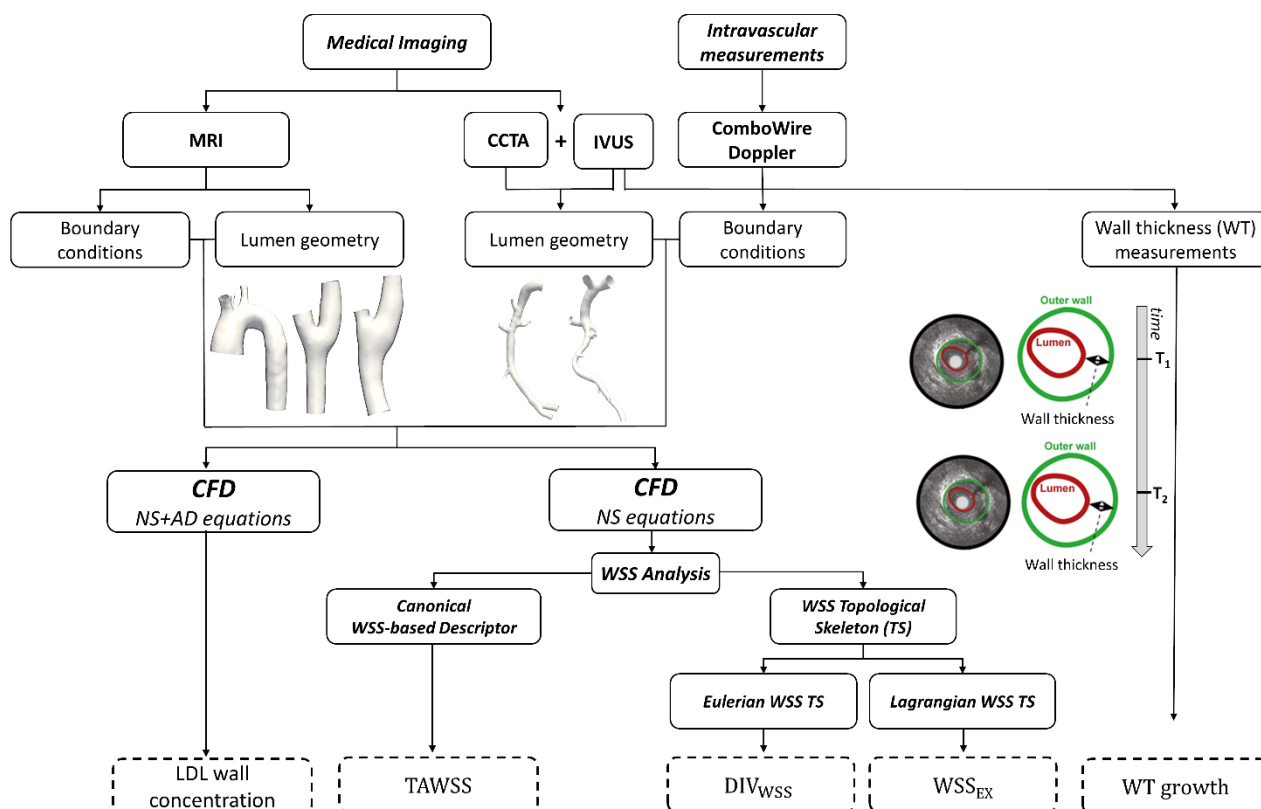


**Figure 2. Explanatory sketch of WSS contraction regions.** A) Typically, the WSS topological skeleton in contraction configuration (WSS unstable manifold, blue line) underlies an arrangement of the near-wall velocity streamlines (black dashed arrows) highlighting the existence of a diffusive boundary layer (grey area). B) Near-wall trajectories of biochemicals accumulate towards the WSS contraction region (blue area), leading to elevated concentrations. The contraction region approximates the unstable critical line (blue line).

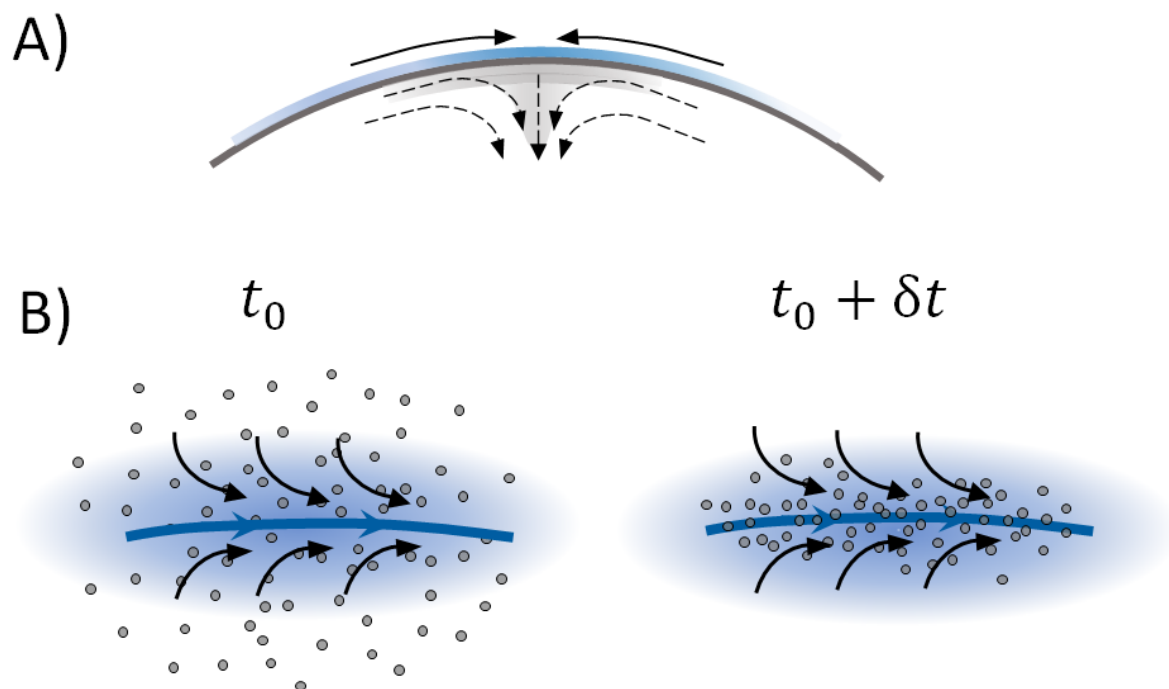


**Figure 3. LDL concentration polarization profile vs. WSS-based hemodynamic quantities.** Luminal distributions of LDL uptake ( $C_W/C_0$ ) and WSS-based quantities (TAWSS,  $DIV_{WSS}$ , and  $WSS_{EX}$ ) for all investigated arterial models. Two different views for each model are displayed. Side branches of the coronary models are not shown.

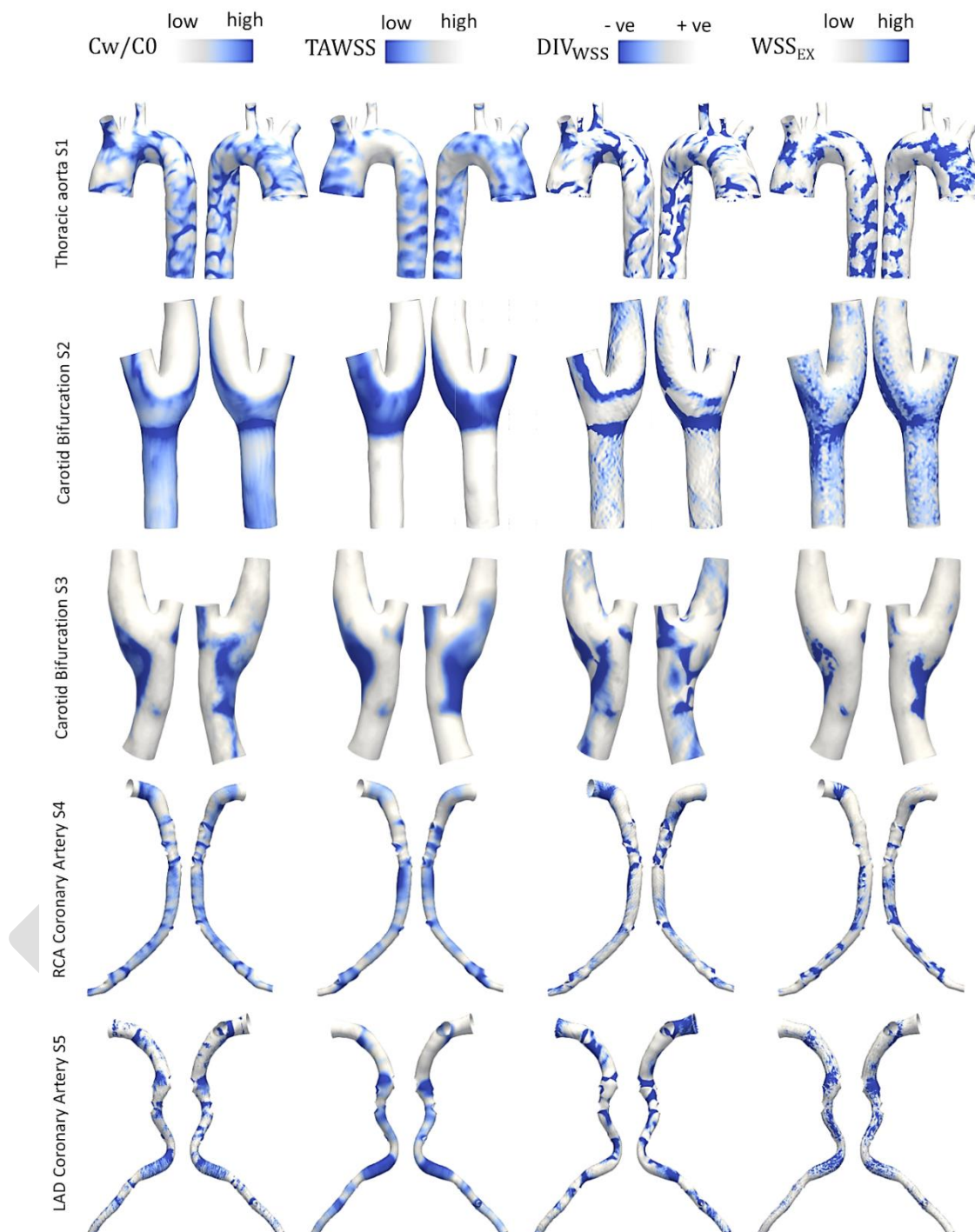


**Figure 4. LDL concentration polarization profile vs. WSS-based hemodynamic quantities along two luminal cross-sections.** Distribution of LDL uptake ( $C_W/C_0$ ) and of the WSS-based quantities (TAWSS,  $DIV_{WSS}$ , and  $WSS_{EX}$ ) along the two luminal cross-sections (labelled section 1 and 2, respectively) characterized by the highest values of LDL concentration polarization for all investigated arterial models. Side branches of the coronary models are not shown.

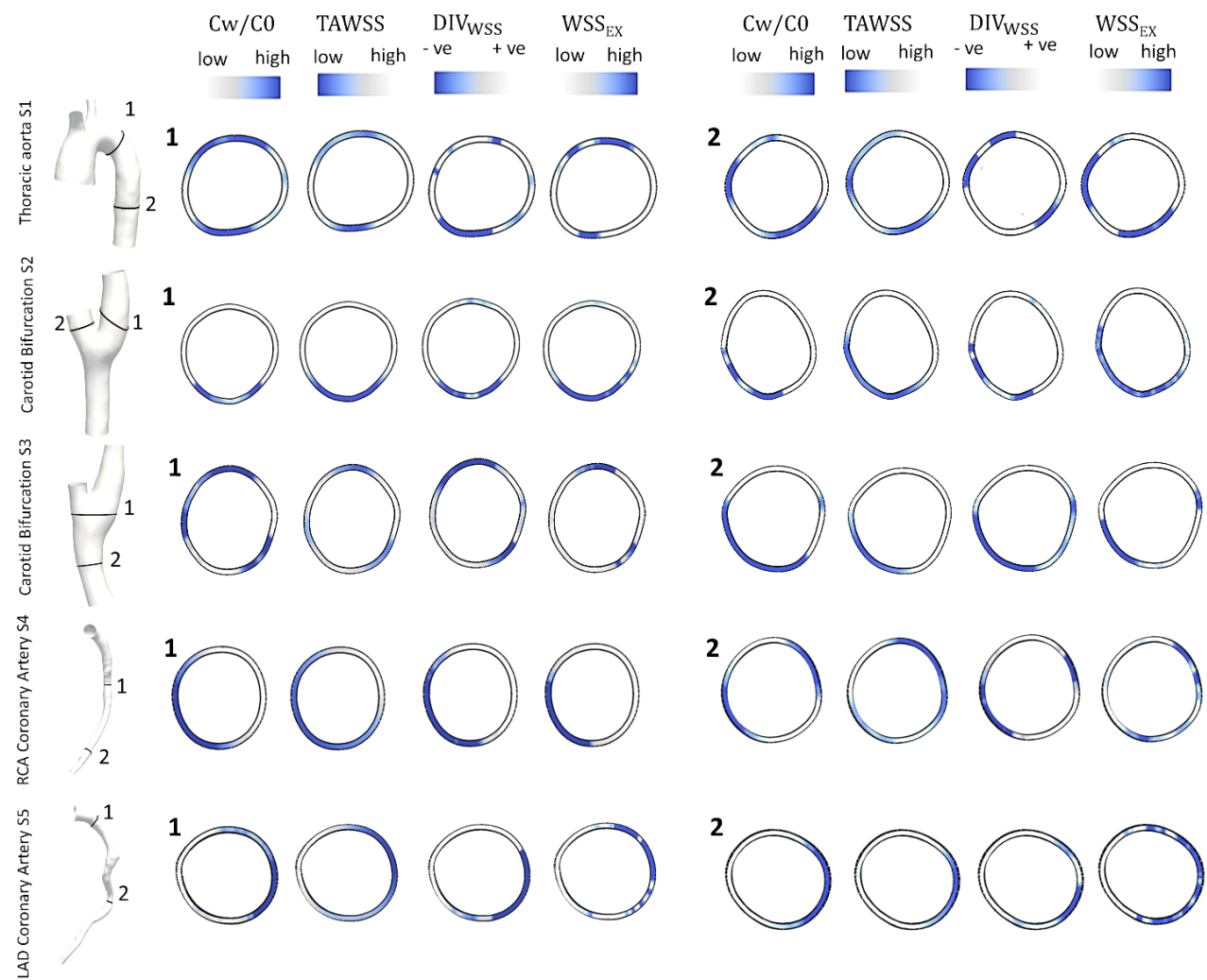


**Figure 5. Co-localization between LDL uptake and hemodynamic quantities.** Visual representation of the spatial overlap of the luminal surface areas exposed to low WSS (TAWSS10), WSS contraction action (DIV10), and high near-wall stagnation (WSSEX90) with regions where LDL uptake is high (LDL90, delimited by black lines) for all investigated models. Two different views for each model are displayed. Side branches of the coronary models are not shown.

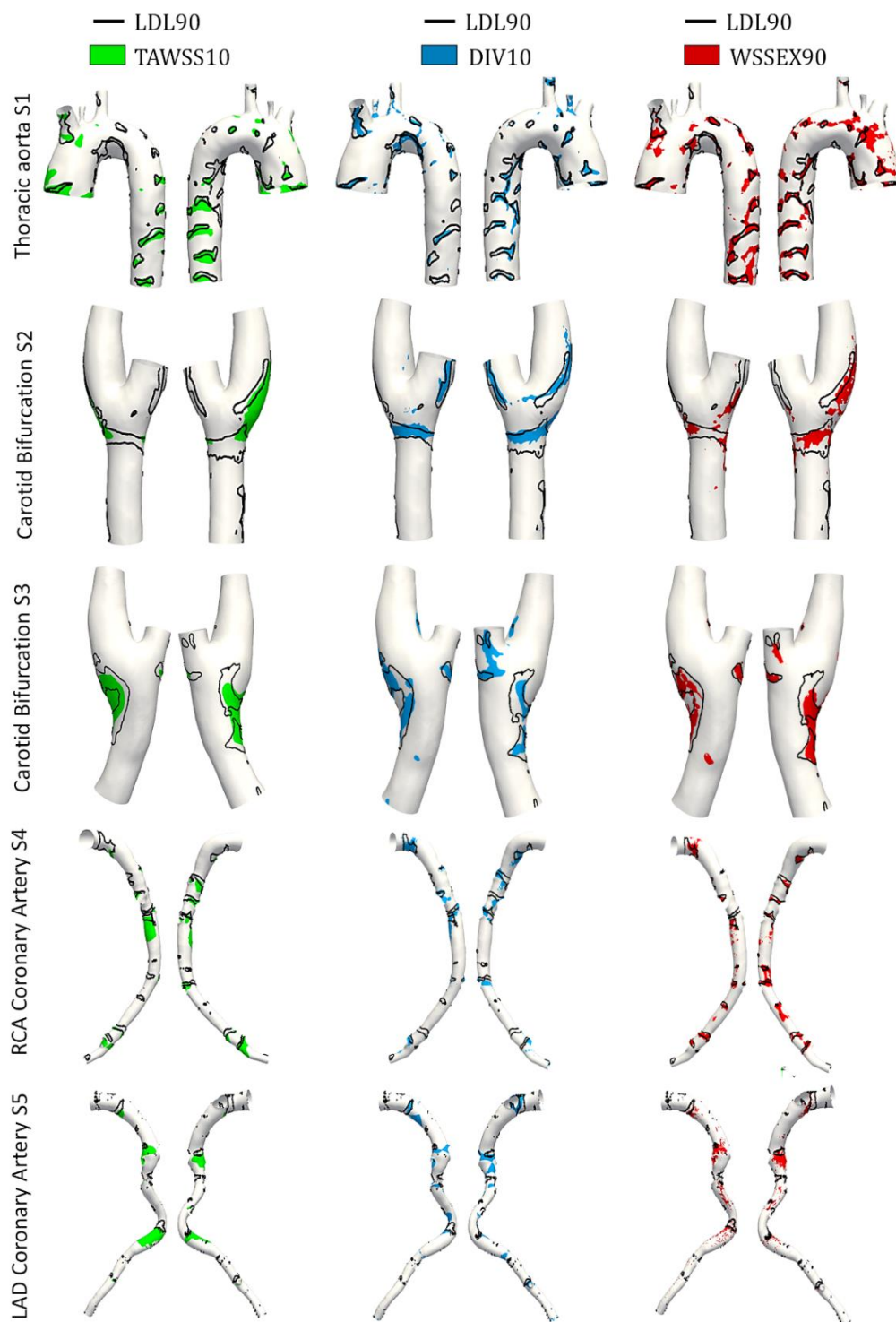


**Figure 6. Maps of LDL concentration profile, WSS-based quantities and wall thickness (WT) growth for the two human coronary artery models.** Luminal distributions of LDL ( $C_W/C_0$ ), WSS-based quantities (TAWSS,  $DIV_{WSS}$ , and  $WSS_{EX}$ ), and wall thickness growth ( $\Delta WT/WT_1$ ) on the two coronary artery models S4 and S5. The regions of interest exhibiting high, extended wall thickness growth along each vessel are emphasized by the arrows. Overall, regions of the arterial wall with high WT growth co-localize with high LDL concentration regions, low TAWSS, negative  $DIV_{WSS}$  and high  $WSS_{EX}$  regions. This confirms that the computational approach adequately identifies locations of possible lesion growth and is effective in unveiling potential links between local hemodynamics and adverse biological events. Side branches of the coronary models are not shown.

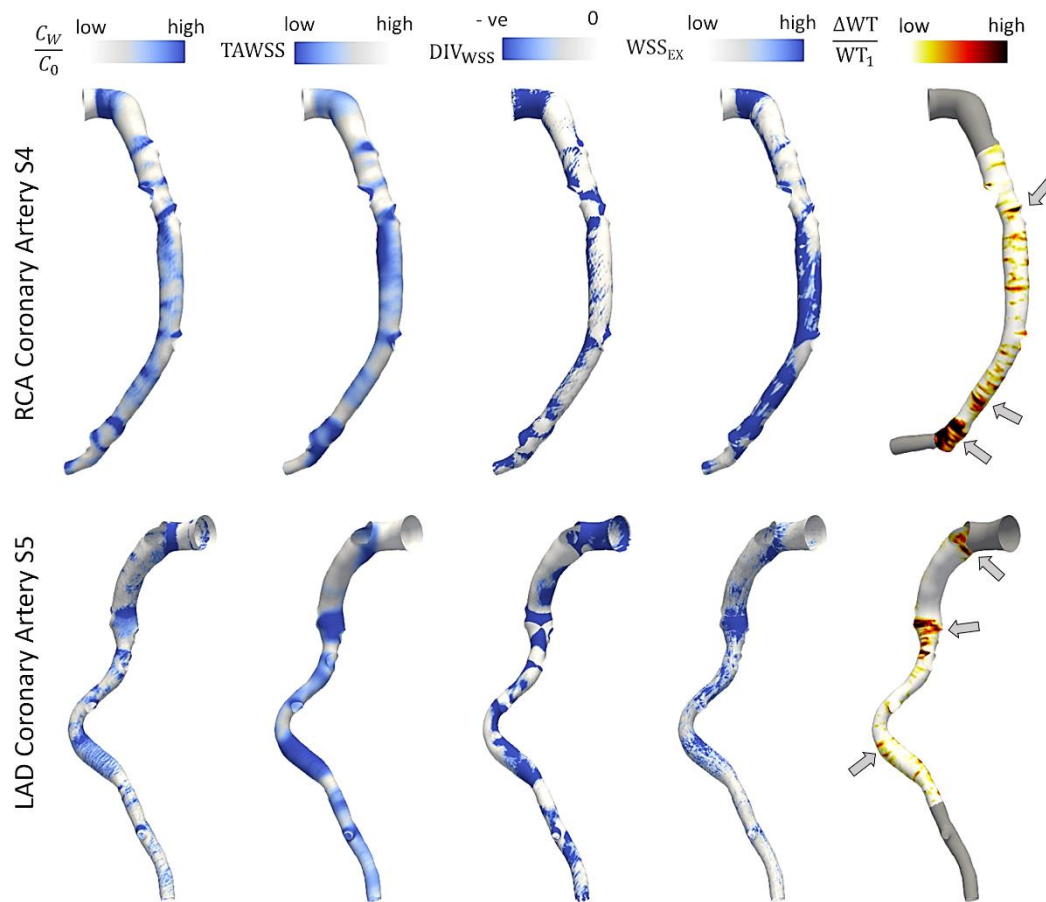




**Figure 7. Schematic of the main findings of the study.** The performance of the investigated WSS-based quantities in providing effective computational templates of the LDL concentration polarization profiles at the arterial luminal surface was evaluated in terms of computational cost vs. accuracy. The computational cost included both the simulation and the post-processing costs. Accuracy is intended as the capability in localizing luminal surface areas prone to LDL concentration polarization, as given by the similarity index. The colour coding represents the trade-off between computational cost and accuracy by a qualitative combination of both.

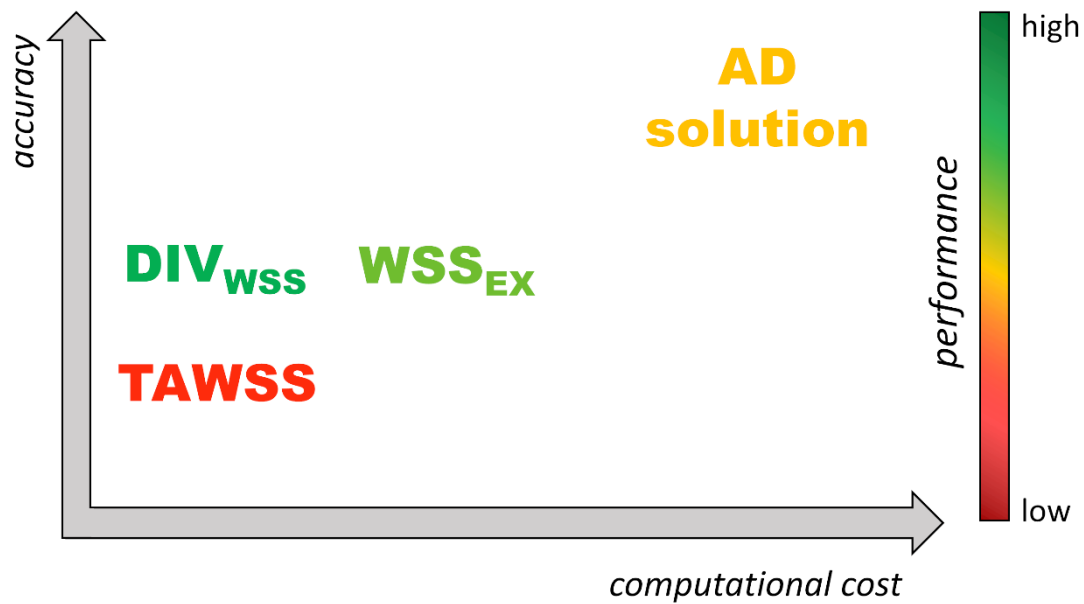


**Table 1. Summary of the input data used to build up the computational models.** Medical imaging techniques used in this study to reconstruct 3D geometries of human vascular districts and vessel-specific measured data available for NS inflow and outflow boundary conditions.

Vessel	Medical Imaging	Measured data available for NS inflow BCs	Measured data available for NS outflow BCs
<b><i>Thoracic aorta</i></b>	4D flow MRI images  (Morbiducci et al., 2009; Volonghi et al., 2016)	4D flow MRI-based measured 3D velocity profile along the cardiac cycle  (De Nisco et al., 2018; Morbiducci et al., 2013)	Instantaneous flow rate waveforms at the supra-aortic vessels  (De Nisco et al., 2018; Morbiducci et al., 2013)
<b><i>Carotid bifurcations</i></b>	CE-MRA  (Gallo et al., 2018; Hoi et al., 2010; Steinman et al., 2002)	2D PC-MRI-based flow rate waveform  (Gallo et al., 2016, 2018)	Instantaneous flow rate waveform at the internal carotid artery  (Gallo et al., 2016, 2018)
<b><i>Coronary arteries</i></b>	CCTA and IVUS  (De Nisco et al., 2021; Hartman et al., 2020)	Combwire Doppler-based velocity profiles along the cardiac cycle  (De Nisco et al., 2021; Hartman et al., 2020)	Flow split measured at multiple locations in the main branch along the cardiac cycle  (De Nisco et al., 2021; Hartman et al., 2020)

NS: Navier-Stokes; BCs: boundary conditions; MRI: magnetic resonance imaging; CE-MRA: contrast enhanced magnetic resonance angiography; PC-MRI: phase contrast MRI; CCTA: computed tomography coronary angiography; IVUS: intravascular ultrasound.



**Table 2. Summary of the WSS-based quantities adopted in this study and their physical/biological implications.** Hemodynamic quantities considered in the study with their biomechanical link with transport of biochemicals in arteries

<i>WSS-based luminal surface area indicating increased risk of biological adverse events</i>	<i>Threshold values for luminal surface area identification</i>	<i>Implications for luminal surface area indicating increased risk of biological adverse events</i>
Luminal surface area exposed to low TAWSS (TAWSS10)	10 <sup>th</sup> percentile of TAWSS distribution	<ul style="list-style-type: none"> <li>• increases endothelial permeability</li> <li>• affects the flux of biochemicals close to the wall</li> <li>• reflects the presence of a thickened diffusive boundary layer</li> </ul>
Luminal surface area exposed to high WSS exposure time (WSSEX90)	90 <sup>th</sup> percentile of WSS <sub>EX</sub> distribution	<ul style="list-style-type: none"> <li>• reflects high near-wall biochemicals' residence time</li> <li>• reflects the presence of a thickened diffusive boundary layer</li> </ul>
Luminal surface area exposed to negative values of normalized WSS divergence (DIV10)	10 <sup>th</sup> percentile of DIV <sub>WSS</sub> distribution	<ul style="list-style-type: none"> <li>• identifies attraction of biochemicals near-wall</li> <li>• identifies flow separation regions</li> <li>• reflects the presence of a thickened diffusive boundary layer</li> </ul>

**Table 3. Co-localization analysis.** Similarity Index values assessing the co-localization between luminal surface areas exposed to high LDL uptake (LDL90) with respect to low WSS (TAWSS10), WSS contraction regions (DIV10), and high near-wall stagnation (WSSEX90).

	<i>Similarity index of LDL90 to:</i>		
	<b>TAWSS10</b>	<b>DIV10</b>	<b>WSSEX90</b>
Thoracic aorta S1	0.33	0.46	0.48
Carotid bifurcation S2	0.19	0.49	0.35
Carotid bifurcation S3	0.50	0.53	0.57
Right coronary artery S4	0.23	0.35	0.45
Left anterior descending coronary artery S5	0.17	0.24	0.24

**Table 4. Quantitative indication of the computational cost.** Number of cardiac cycles required for each investigate model to ensure convergence of the unsteady Navier-Stokes (NS) solution; additional number of cardiac cycles required to ensure convergence of the advection-diffusion (AD) solution.

<i>Number of cardiac cycles ensuring convergence of:</i>		
	<i>NS solution</i>	<i>AD solution</i>
<i>Thoracic aorta S1</i>	4	10
<i>Carotid bifurcation S2</i>	3	5
<i>Carotid bifurcation S3</i>	3	5
<i>Right coronary artery S4</i>	2	3
<i>Left anterior descending coronary artery S5</i>	3	4